Pergamon

PII: S0191–8141(97)00104–1

Journal of Structural Geology, Vol. 20, No. 5, pp. 573 to 585, 1998

0191-8141/98 $19.00 + 0.00

From finite strain data to strain history: a model for a sector of the Ligurian Alps, Italy

S. SENO, G. DALLAGIOVANNA and M. VANOSSI

Dipartimento di Scienze della Terra, University Degli Studi di Pavia, via Ferrata 1, 27100, Pavia, Italy

(*Received* 14 *April* 1997; *accepted in revised form* 1 *October* 1997)

Abstract—Bulk strain measurements were made in a Penninic sector of the Ligurian Alps. Previous detailed mapping, supported by petrographic and structural analyses, had shown that the oldest (D_1), complex Alpine episode produced km-scale sheath-like folds, involving basement and cover, before the activation of a set of thrusts leading to nappe superposition. By combining all data, a kinematic model has been developed into which the subsequent deformation steps have been set. In particular, total strain constraints led to the suggestion of a combination of relatively low values of pure shear and simple shear for the genesis of the sheath-like folds. A computer simulation has proved that this suggestion is tenable. The model was then used to factor the bulk strain into increments—starting from the diagenetic compaction of the cover, up to the last 'late D_1' phase—necessary to obtain results that compare well with the finite strain data. Some theories were also deduced on the possible attitude of the pre-Alpine schistosity in the basement rocks at the beginning of Late Variscan times. © 1998 Elsevier Science Ltd. All rights reserved

INTRODUCTION

A detailed cartographic and structural study was recently performed (Dallagiovanna *et al*., 1997b) in the Barbassiria area, which is located in the Penninic zone, and specifically in the Briançonnais domain, of the Ligurian Alps. Four superposed Alpine tectonic units were mapped and special attention was paid to their complicated deformational history, which began with the birth of sheath-like folds in the lower unit.

The present paper presents a model for the generation of such folds and uses finite strain measurements to check the model and to reconstruct the most probable strain path during the first, polyphase, Alpine episode of deformation. Moreover, some information is deduced on the possible attitude of the pre-Alpine schistosity in the basement rocks at the beginning of Late Variscan times.

Besides local results, we suggest that the approach and methods used are applicable to other tectonically complex situations.

GENERAL STRUCTURAL SETTING

The information outlined in this section mainly comes from Cabella *et al*. (1991), Cortesogno *et al*. (1993, 1995) and Dallagiovanna *et al*. (1997b). The four superposed units that have been mapped (Fig. 1) are thought to come from progressively inner palaeogeographic domains, namely the Briançonnais and Piedmont sectors. In particular, the two lower units—(from the bottom: the Mallare unit (Ma) and the Pamparato–Murialdo unit (Pa)—are assigned to the intermediate-inner Briançonnais domain. They occupy the largest part of the area, where Ma crops out below Pa. The present paper deals mainly with Ma, on which strain measurements were performed.

Ma and Pa stratigraphic sequences

The Ma series begins with a metamorphic, originally mainly rhyolitic, pre-Namurian basement ('Barbassiria Orthogneisses'), which was affected by both Variscan and Alpine orogenises. Its cover is made up of Upper Carboniferous metavolcanics ('Case Lisetto Metarhyolites' 0–80 m) and metasediments ('Ollano Formation' about 200 m). The upper part of the sequence was tectonically transported forward (i.e. towards the southwest) during the emplacement of Pa on Ma.

Although of differing facies and age, a pre-Namurian orthogneissic basement and an Upper Carboniferous cover (mainly represented by phyllites and meta-andesites) also constitute the Pa series, which is locally completed at the top by a very 'reduced' Upper Cretaceous, calcareous sedimentary cover.

Alpine folding phases and related metamorphic conditions

The Mallare and Pamparato–Murialdo units were involved in three main superimposed folding phases (D_1, D_2 and D_3) which developed, with decreasing intensity, in progressively higher structural levels. Only the first two Alpine folding episodes are associated with significant metamorphic parageneses. S_1 schistosity developed under high-pressure conditions ($P \approx 0.8$ GPa, $T \approx 350°C \pm 25°C$ in the Ma and Pa units), while S_2 foliation is characterized by a decompres-

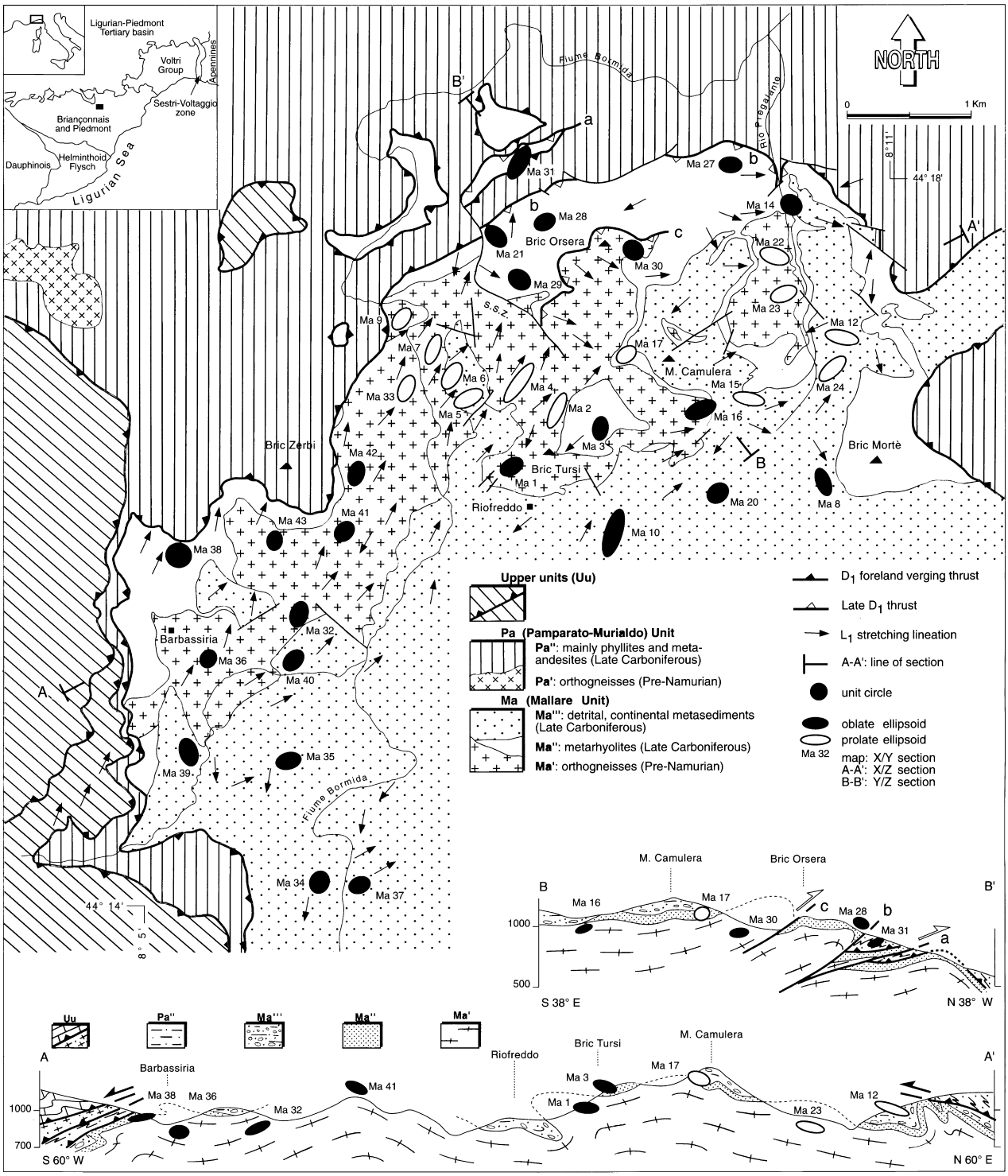

Fig. 1. Map and cross-sections of the Barbassiria area, showing finite strain data.

sional evolution ($P \approx 0.55$ GPa), possibly accompanied by a slight temperature increase.

In the Mallare unit, the D_1 phase produced some gently inclined, km-scale folds, involving both basement and cover. Besides fold vergence, the tectonic transport direction is indicated by: (i) a stretching lineation L_1, trending NE–SW (Fig. 2); (ii) S–C systems affecting the thin metasedimentary layers in the basement, and the very frequent thin mylonitic shear bands in the gneisses, both showing a 'top-to-the-southwest' shear sense; and (iii) σ and δ structures (Ramsay and Huber, 1987, p. 633) around rotated porphyroclasts, in gneisses as well as in metarhyolites.

The hinge lines of D_1 folds are curved. For the largest of these folds (the Bric Tursi anticline and the underlying Rio Freddo syncline: Fig. 1, cross-section A–A′; Fig. 3), the attitude of the L_{01} bedding–S_1 schistosity intersection lineation in the Upper

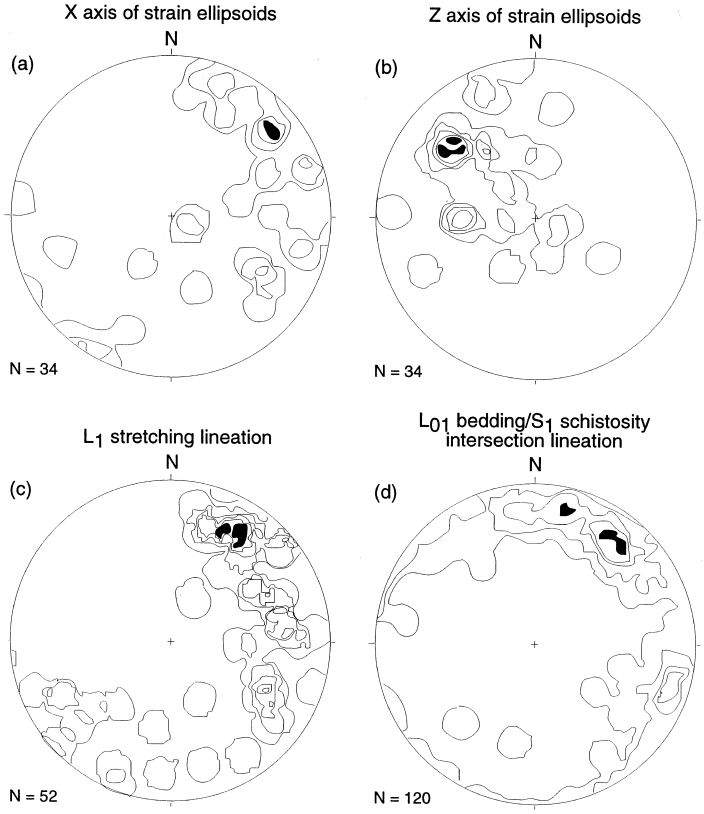

Fig. 2. Density diagrams (step function, Schmidt net, lower hemisphere). Contour interval is 2% per 1% area.

Carboniferous metasediments (Fig. 2, plot d) shows a hinge line variation greater than 90°. Hence, the fold displays a sheath-like geometry (Ramsay and Huber, 1987; Skjernaa, 1989). All over the mapped area—apart from a local exception connected with the subsequent 'late D_1' episode—the stretching lineation L_1 is not deflected (Fig. 1): this indicates that the curvature of the hinge line was acquired during the D_1 folding phase and that it cannot be ascribed to a later folding event.

Both the map and cross-sections (Fig. 1) clearly indicate that the superposition of Pa on Ma was achieved only after the first folding phase, along a low-angle thrust plane which cuts the D_1 folds affecting the Ma

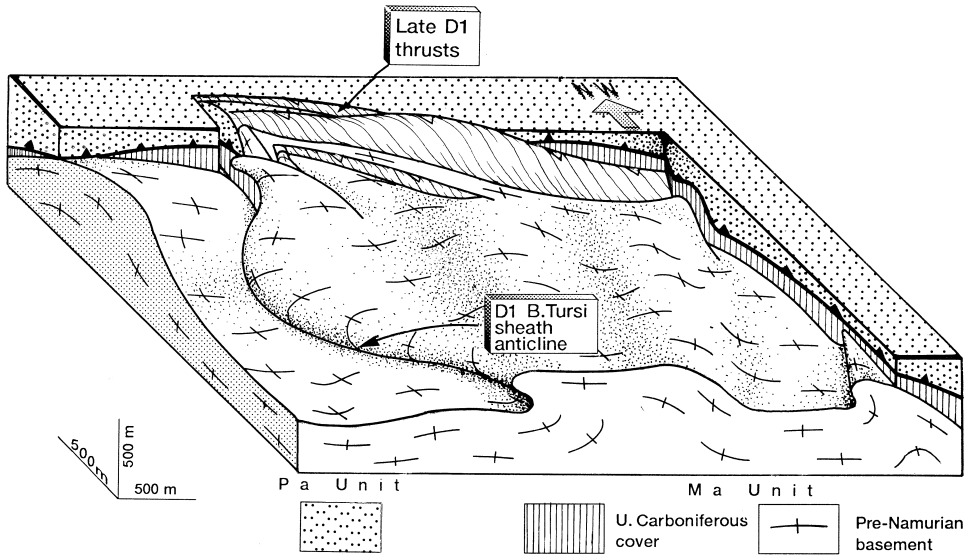

Fig. 3. Schematic three-dimensional presentation of the principal km-scale structures of the Barbassiria area. The D_1, gently inclined, SW-verging sheath-like folds, the late D_1 thrusts and the 'dome-and-basin' interference pattern (produced by superimposition of the D_3 episode on $D_1 + D_2$ structures) are outlined. The front view approximately coincides with the A–A′ cross-section in Fig. 1, while the B–B′ cross-section runs approximately at right angles along the central sector of the block diagram.

unit. The nappe stacking was in turn followed by the development of a new approximately NW-verging deformation, indicated by a thrust system, accompanied by fault propagation folds and involving both Ma and Pa units. A transfer fault confines these structures to the northeastern sector of the area (Fig. 1, map and cross-section B–B′; Fig. 3). Being affected by the D_2 foliation, they have been ascribed to the first, complex episode and referred to as the 'late D_1' phase.

The D_2 phase has produced open to moderately tight folds, associated with a well-developed compressional crenulation cleavage (S_2); the folds are characterized by an overall NW-directed, not very prominent, vergence; their mean trend is 050°.

The last phase (D_3) produced folds with subvertical axial planes, mainly trending NW or NNW. It also produced large spectacular, asymmetrical 'dome-and-basin' interference patterns.

FINITE STRAIN DATA

Finite strain analysis was carried out on the Ma unit, using the above-mentioned three different lithologies: (1) pre-Namurian orthogneisses, characterized by abundant K-feldspar megacrysts and lenticular quartz; (2) rhyodacitic meta-ignimbrites; and (3) fluvial–lacustrine meta-conglomerates. Bulk strain determination was performed using the Fry centre-to-centre method (Fry, 1979; Hanna and Fry, 1979) and the $R_f\phi$ method (Ramsay, 1967; Dunnet, 1969; Lisle, 1977).

The Fry method was used in the case of quartz and feldspar grains from the gneisses and metarhyolites, and with clasts from the Carboniferous metaconglomerates, showing a competence greater than their matrix. The effects of particle size variations were partly eliminated using the normalized analysis proposed by Erslev (1988). The $R_f\phi$ method was preferred in the case of conglomerates showing only a weak deviation of schistosity around clasts.

Measurements were carried out using enlarged photomicrographs of thin sections, or directly from polished hand-sample sections; the contours of strain markers were traced on transparent overlays on the wetted slab surfaces and the tracings were then digitized. A minimum of 40–120 objects were digitized from each section, and calculations performed using

Table 1. Strain data and attitude of strain ellipsoid axes in the Mallare unit (Ma). Orth. = orthogneisses from pre-Namurian basement; Rhyol. and Congl. = metavolcanics and metasediments from Upper Carboniferous cover. $K = \ln(X/Z)/\ln(Y/Z)$. X, Y and Z are normalized to constant volume ellipsoid equal to $4\pi/3$; (az/pl) = (azimuth/plunge)

Sample	Lithology	X/Y	X/Z	Y/Z	K	X	Y	Z	X (az/pl)	Y (az/pl)	Z (az/pl)
Ma1	Orth.	1.54	2.41	1.56	0.97	1.54	1.00	0.64	062/04	156/22	310/65
Ma2	Orth.	3.04	4.23	1.39	3.38	2.34	0.77	0.55	026/01	293/10	122/80
Ma3	Rhyol.	1.45	2.24	1.54	0.86	1.48	1.02	0.66	008/24	161/63	273/10
Ma4	Orth.	3.65	7.23	1.98	1.89	2.98	0.82	0.41	035/07	307/13	098/74
Ma5	Congl.	2.25	3.89	1.73	1.47	1.97	0.96	0.53	065/37	203/43	317/23
Ma6	Congl.	1.86	3.03	1.62	1.29	1.78	0.95	0.58	032/30	123/02	212/60
Ma7	Orth.	2.33	3.01	1.29	3.32	1.91	0.82	0.63	022/16	120/32	270/52
Ma8	Congl.	2.02	2.70	1.34	2.41	1.76	0.87	0.65	159/12	046/61	255/25
Ma9	Orth.	1.66	2.27	1.37	1.61	1.55	0.93	0.68	049/16	141/08	260/70
Ma10	Orth.	2.85	9.67	3.39	0.86	3.02	1.06	0.31	197/37	340/43	090/20
Ma12	Congl.	2.61	4.00	1.53	2.26	2.18	0.84	0.55	102/20	184/00	280/80
Ma14	Rhyol.	1.30	2.43	1.87	0.42	1.46	1.12	0.60	123/26	222/18	345/55
Ma15	Congl.	2.65	3.15	1.19	5.59	2.03	0.77	0.64	101/79	261/10	352/04
Ma16	Orth.	1.84	4.41	2.40	0.70	2.01	1.09	0.46	067/33	186/39	309/34
Ma17	Rhyol.	1.47	1.74	1.18	2.33	1.37	0.93	0.79	135/22	237/18	005/60
Ma20	Congl.	1.24	2.19	1.77	0.38	1.40	1.13	0.64	232/38	118/28	002/39
Ma21	Rhyol.	1.54	2.83	1.84	0.71	1.63	1.06	0.58	131/80	249/02	340/20
Ma22	Orth.	1.97	3.62	1.84	1.11	1.92	0.97	0.53	106/13	221/57	010/30
Ma23	Orth.	1.87	2.84	1.52	1.50	1.75	0.93	0.61	071/13	286/80	160/02
Ma24	Congl.	2.37	4.02	1.70	1.63	2.11	0.90	0.53	230/21	136/10	066/23
Ma27	Rhyol.	1.42	2.10	1.49	0.88	1.44	1.02	0.68	090/37	189/12	294/50
Ma28	Rhyol.	1.40	2.10	1.50	0.83	1.43	1.02	0.68	253/28	359/23	120/50
Ma29	Rhyol.	1.29	2.77	2.14	0.33	1.53	1.19	0.55	122/35	217/08	318/55
Ma30	Orth.	1.18	2.36	2.00	0.24	1.39	1.18	0.59	120/42	218/06	315/45
Ma31	Rhyol.	2.14	5.50	2.57	0.81	2.27	1.06	0.41	212/60	072/26	335/15
Ma32	Orth.	1.43	3.03	2.12	0.48	1.63	1.14	0.54	200/25	092/29	320/40
Ma33	Orth.	1.81	2.69	1.48	1.50	1.70	0.94	0.63	025/28	134/34	265/55
Ma34	Congl.	1.13	2.50	2.21	0.15	1.41	1.25	0.56	210/08	116/18	320/70
Ma35	Congl.	1.57	2.80	1.78	0.78	1.63	1.04	0.58	077/54	198/20	300/25
Ma36	Orth.	1.13	1.45	1.28	0.49	1.18	1.04	0.81	040/00	130/60	310/30
Ma37	Congl.	1.35	2.02	1.49	0.75	1.39	1.03	0.69	072/10	172/42	330/45
Ma38	Rhyol.	1.11	4.25	3.84	0.08	1.67	1.51	0.39	276/06	008/18	160/70
Ma39	Congl.	1.50	8.94	5.99	0.23	2.36	1.57	0.26	160/50	054/14	310/35
Ma40	Congl.	1.42	2.63	1.85	0.57	1.55	1.09	0.59	048/12	160/60	310/25
Ma41	Orth.	1.28	2.22	1.73	0.45	1.41	1.11	0.64	050/24	166/45	300/35
Ma42	Orth.	1.51	2.55	1.69	0.78	1.56	1.04	0.61	020/10	115/28	270/50
Ma43	Orth.	1.20	1.52	1.26	0.79	1.22	1.02	0.80	012/10	110/38	270/50

an automated procedure with the program 'INSTRAIN' (Erslev, 1988; Erslev and Ge, 1990).

The strain ellipsoid was determined by means of two sections cut parallel and perpendicular to the main fabric elements (usually S_1) or by means of any three non-perpendicular sections, with at least one set of strain data obtained in one of the principal planes of strain; in this case the ellipsoid calculation was made using the program 'MacStrain' (written by Kanagawa), based on Wheeler's (1986) and Milton's (1980) methods.

Strain data and the orientations of strain ellipsoid axes are listed in Table 1; X axis plunge is also represented in Fig. 2. From the map (Fig. 1) and the Flinn diagram (Fig. 4) the following main trends are apparent:

1. the ellipsoids vary from oblate (apparent flattening) to prolate (apparent constriction) shapes, even though most of the data plot in the apparent flattening field;
2. the prolate ellipsoids are only present in the north-eastern sector, where they appear along a narrow belt trending NE–SW, just south of the 'late D_1' thrusts. The metarhyolites are poorly represented in this belt and most of the metarhyolite samples fall in the apparent flattening field;
3. the pattern in Fig. 4 is not simple; it shows a considerable scatter, with no separation among samples from the orthogneiss and metaconglomerate units.

Ellipticity varies in the XY principal plane between 1.11 and 3.65, and in the XZ plane between 1.74 and 9.67, with an apparent lack of correlation with structural level (i.e. proximity to the main thrust at the top of the Ma unit). The shape of the finite ellipsoids is not influenced by later deformation (D_2): samples were selected from sites where no S_2 fabric was observed to be affecting S_1 schistosity and the XY principal plane is parallel to S_1. Moreover, there is a strong tendency (Fig. 2, compare plots a and b) for the X axis to align subparallel to the trend of the L_1 stretching lineation, as deduced from elongated clasts of metaconglomerates or from quartz–feldspar porphyroblasts from the gneisses. Both the X axes and the L_1 lineation show an average NE–SW trend, and where L_1 deviates from this direction, the X axes display a similar pattern.

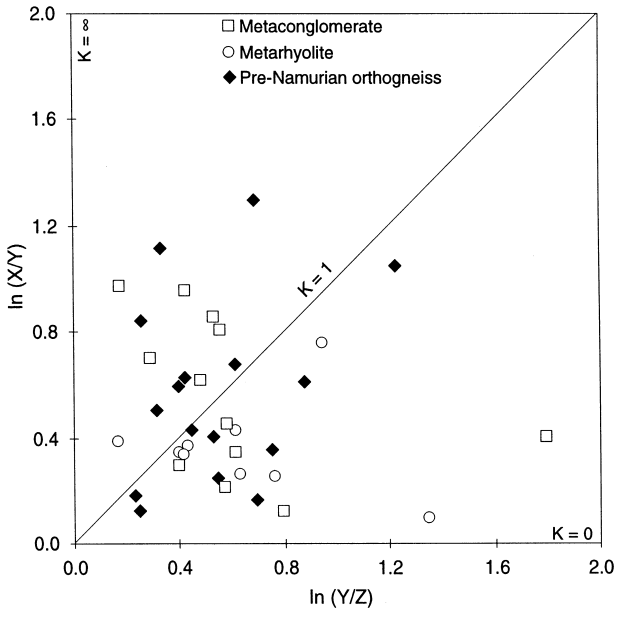

Fig. 4. Flinn plot of measured strain ellipsoids.

The orientation of X axes with respect to the main D_1 folds depends on the position along the fold hinge: for instance, the Bric Tursi anticline and the Rio Freddo underlying syncline (cross-section A–A′ in Figs 1 & 3) are non-cylindrical with a pronounced hinge line bend, and the angle between the X direction and the fold axes varies from 90° to 20° (Fig. 2, compare plots a and d).

STRAIN FACTORIZATION

To investigate the genesis of our sheath-like D_1 folds and to explain the observed bulk strain, we will discuss the most probable strain path for pre-D_2 deformation. The choice of the sequence of steps first depends on the regional geological constraints that are presented in the following paragraphs. In the next section, the same sequence of episodes will be treated by means of deformation tensors, and the results of strain path simulations will be compared with the measured finite strain.

For factorization purposes we have disregarded both the ellipsoids from the pre-Namurian basement (because of their longer and less well known history) and those affected by the 'late D_1 phase'. All the ellipsoids that have been taken into account are of the oblate type and may be regarded as resulting from two increments of strain acquired during diagenesis and the later, complex, D_1 Alpine episode.

Diagenesis

Regional data (Vanossi *et al.*, 1986; Vanossi, 1991) indicate that the total thickness of the stratigraphic sequence originally lying on the Upper Carboniferous volcanics and sediments was probably around 1.5–2 km. With such a load, the initial porosity of rhyolitic volcanics is highly reduced (Fisher and Schmincke, 1984) and the loss of volume can be estimated at about 15–20%. These same values are indicated (Rittenhouse, 1971; Loup, 1992) for compaction of heterometric sediments similar to ours. The volume reduction is obviously accomplished mainly by shortening along the vertical axis; the possibility of a concomitant axial symmetrical extension in the horizontal plane depends on many factors, but mainly the lateral confinement. On this basis, we have assumed

that diagenesis produced the same loss of volume in the volcanics and sediments. Moreover, as both the rhyolites (which form a discontinuous layer) and the sediments (fluvial–lacustrine) represent laterally confined bodies, we have expressed the total volume loss as a vertical shortening.

As will be seen, the range of values for the first strain increment that best combines with subsequent increments to give the finite strain values lies between 10 and 25% of shortening, and this is in agreement with the above figures from the literature.

Sheath-like fold development

As generally is the case, the strain path derived from regional geological constraints is not unique. The solution suggested below has been selected because it seems to combine fairly well the geological framework and the bulk strain data.

The metamorphic conditions indicate that the D_1 folding of Ma and Pa was accomplished at a depth of about 30 km, which was probably reached along an inclined shear zone; on the basis of the kinematic indicators, this has been assumed to have a hindward (i.e. northeastward) dip. Before the Alpine deformational episodes, Pa and Ma represented two adjacent sectors of the Briançonnais domain (Vanossi *et al.*, 1986). As Pa was thrust upon Ma only after the D_1 folding episode, it follows that both units probably kept their original contiguity until they were piled up. At a regional scale (Vanossi, 1991), D_1 fold vergence of both units is towards the southwest. The total outcrop extent of both units in the Ligurian Alps in this direction is about 30 km; the amount of displacement of Pa on Ma in the direction of tectonic transport, such as can be measured on a regional map, is at least 11 km.

Assuming that the petrographic methods that were employed to estimate thermobavometric conditions carry an error of $\pm 10\%$, the shear zone dip should have been about 5–8°, in order to keep Ma and Pa adjacent at a suitable depth for their metamorphism (Fig. 5a). Such a low value of dip seems to be common in intra-continental 'subduction' zones, as supported, for instance, by seismic profiles of the Penninic nappes of the Alps (Frei *et al.*, 1990).

At the end of the D_1 episode, the pre-existing surfaces (S_0) had been folded and more or less completely transposed on to Alpine S_1 planes; the angle between these two sets of surfaces on the limbs of the fold rarely exceeds 5–10°.

From the map and cross-section it can be deduced that the angle between S_1 and the thrust plane ('th') along which Pa was transferred onto Ma is about 15–20°. Taking account of the temperature data, the inclination of this plane to the shear zone may not have exceeded some 5–10°. On the basis of these assumptions, the inclination of S_1 to the shear zone at the end of the D_1 folding episode may be fixed at about 25–30°; consequently, the angle between S_1 and the horizontal plane would approach 35°. This value, however,

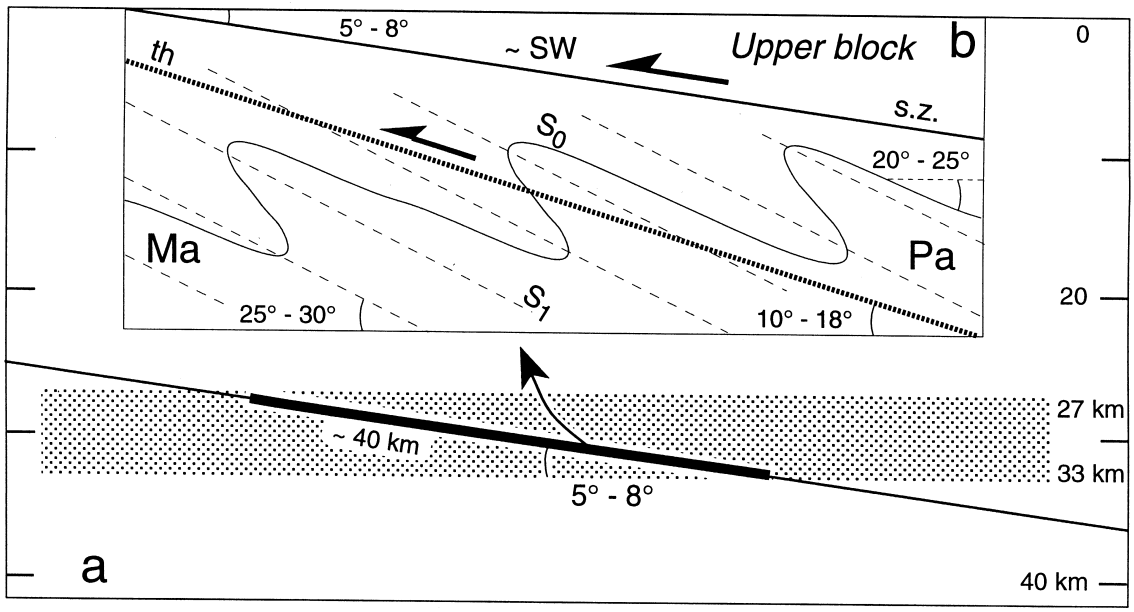

Fig. 5. Inferred inclinations of some sets of surfaces involved in the D_1 episode. (a) Inclination of the shear zone producing D_1 folds and related metamorphism of Pa and Ma units. The value ($\alpha \cong 8°$) is calculated from metamorphic parageneses, indicating a depth of about 30 km ($\pm 10\%$), and from the minimum length ($a \cong 40$ km) of the sector they affect. (b) Schematic vertical section, showing the inferred dip of the different types of surfaces affected by the D_1 folding and overthrusting phase. s.z. = upper boundary of the shear zone; in the considered sector, it is located at a depth of about 30 km; S_0 is the original sedimentary (or pre-Alpine metamorphic) foliation; S_1 is the axial plane schistosity accompanying D_1 folds; th is the attitude of reverse thrusts cutting D_1 folds.

should be slightly lowered, because present measurements indicate that the mean original inclination of the L_1 stretching lineation did not exceed 20–25°.

In conclusion, at the end of the D_1 folding phase, the shear zone and the thrust, as well as S_0 and S_1 sets, had a hinterland dip. As to their inclination to the horizontal, the values that we assume to be the most likely are indicated in Fig. 5(b). According to the above assumptions, the top of the shear zone can be geometrically represented by an inclined plane that separates an upper block from a lower one. In order to generate SW-verging D_1 folds in the lower block (i.e. in Ma and Pa), the relative motion of the upper block must have been towards the southwest.

The hinge line curvature of the D_1 folds recalls the geometry of sheath folds produced by simple shear. A simple shear regime is also deduced from the aforementioned: (i) abundant shear-sense indicators; (ii) the low angle between foliation and bedding; and (iii) the position of the folded unit at the base of a pile of nappes. Cobbold and Quinquis's (1980) model producing sheath folds by simple shear requires a shear zone bounded by two horizontal planes and assumes the following conditions; (i) pre-existing non-cylindrical folds (representing an initial inhomogeneity; the direction of their near-vertical axial planes must be sub-orthogonal to the direction along which the maximum shear stress will act) and (ii) to obtain highly curved hinge lines, the shear strain γ must have a value of 5 or more.

To meet the first of these conditions we chose, among other possibilities, to apply to our region a moderate shortening, producing open, multi-km-scale, asymmetric, non-cylindrical folds. In fact, the compressional stress field that will successfully generate the shear zone might initially have produced a relatively mild deformation such as this.

This hypothetical 'early D_1' episode cannot amount to a more severe folding. Indeed, if this were the case, the amount of shear strain necessary to rotate subvertical limbs to the required inclination would be more than $\gamma = 2$, higher than the value consistent with our strain data. On the other hand, neither these data nor the oblate shapes of the ellipsoids fit the second condition ($\gamma > 5$) of Cobbold and Quinquis's model. Hence, considering the low value of the angle between S_0 and S_1, and in order to account for the depth at which the deformation was accomplished, we considered it reasonable to assume that in the shear zone the strain induced by the SW-directed movement of the upper block developed simultaneously with a pure shear and a simple shear component.

In conclusion, we suggest that the sheath-like folds were generated within an inclined shear zone, at a depth of some tens of kilometres, by the simultaneous superposition of simple and pure shear strain on pre-existing, open, asymmetric, non-cylindrical folds. In this model, the present geometry would have been obtained with values of γ much less than those required by Cobbold and Quinquis's model. As will be seen, it is possible to choose 'reasonable' ranges of values for the two strain increments (corresponding to the 'early D_1' undulation and to the subsequent generation of sheath-like folds by a combination of pure and simple shear) in order to obtain finite strain ellipsoids very similar to those measured. Moreover, computer simulation (see below) shows that sheath-like folds can be produced by the same strain path and the above 'reasonable' ranges of values for the strain increments.

'Late D_1' thrusting episode

Figure 1 shows that the transfer fault bordering the thrust system to the west dies out towards the south, and that similarly the prolate ellipsoids are confined to a restricted area, south of which no evidence of this deformation exists. Hence, this shortening only affected a portion of the mapped region.

The map and strain measurements indicate that shortening is concentrated in two belts: a northern sector, where the prolate ellipsoids are lacking and the shortening is achieved by brittle deformation (thrust system); and a southern sector, indicated by the distribution of the prolate ellipsoids, where shortening is documented by some folds having a subvertical, NE-trending axial plane. Here, the lateral confinement by the transfer fault no longer exists and the belt involved in the shortening is wider than in the northern sector.

From the sense of rotation of the L_1 stretching lineation and the fact that no extensional structures parallel to the thrust-trend exist at the southern margin of the southern sector, it may be argued that the structures cannot simply be due to the northward-directed movement of the shortened block. We suggest that these structures might represent the hinterland-verging part of a 'pop-up'-like structure—oblique to the general D_1 trend—that was generated by a buried, local, transverse obstacle, which was set up during the ongoing foreland-directed tectonic transport. When looking only at their local development, these structures appear as a kind of 'accident' and do not influence the regional tectonic development. Attention has nevertheless been paid to them in order to reconstruct the full strain path for pre-D_2 episodes and to check it against the bulk strain data and the geological structures that were mapped in detail.

In view of this, the following section shows that the calculation of the strain increment associated with the 'late D_1' episode (which is necessarily linked to the collected data, rather than to the relevant kinematic model) leads to results that support (or, at least, do not disprove) the above interpretation.

STRAIN PATH SIMULATION FOR PRE-D_2 EPISODES

To discuss the development of finite strain in light of the above tectonic model, the deformation path was investigated using the strain factorization method, performed by multiplying a series of matrices, each representing a strain increment (Sanderson, 1976; Flinn, 1978; Ramsay and Huber, 1987).

A coordinate system was defined in the deformed state with the z axis vertical, y normal to regional trend of the stretching lineation L_1, and x parallel to it. The finite strain was factored and the deformation path investigated by the sequential multiplication of the following incremental strain matrices:

(i) pre-tectonic compaction (Δ) ranging from 10 to 25% in the z direction as discussed above (matrix M_1);
(ii) coaxial plane strain with 15% of shortening along x (layer-parallel shortening, LPS), related to the early-D_1 open folding (matrix M_2);
(iii) contemporaneous superposition of layer-parallel simple shear and pure shear achieved in a crustal-scale zone (matrix M_3);
(iv) shortening normal to the stretching lineation direction, confined in the northern part of the unit and following the stack of the upper nappes on the Ma (matrix M_4).

In the above-defined coordinate system, vertical compaction is represented in matrix form by

$$M_1 = \begin{bmatrix} 1 & 0 & 0 \\ 0 & 1 & 0 \\ 0 & 0 & 1+\Delta \end{bmatrix} \quad (\Delta \text{ negative}) \qquad (1)$$

and LPS (pure shear) parallel to x by

$$M_2 = \begin{bmatrix} \sqrt{\lambda} & 0 & 0 \\ 0 & 1 & 0 \\ 0 & 0 & \frac{1}{\sqrt{\lambda}} \end{bmatrix} \quad (\lambda < 1). \qquad (2)$$

The values for the longitudinal strain and simple shear to be introduced in matrix M_3 have been selected in order to fit the bulk strain data. Following Coward and Kim's (1981) and Sanderson's (1982) method, we used the diagram of ellipticity against angle between the shear zone and the X axis of the ellipsoid. On these diagrams (Fig. 6) we plotted the prolate ellipsoids from the Ma cover and two sets of curves: equal extension ($\sqrt{\lambda}$) and constant shear strain (γ). While in both Coward and Kim's and Sanderson's works these two sets of lines have been calculated starting from the deformation of an initial sphere, in our plot we have also to consider the two initial increments (volume reduction due to compaction and LPS). Therefore, matrix M_3 was first sequentially multiplied by M_1 and M_2, and the tensor $Q = M_3 \cdot M_2 \cdot M_1$ was then used to calculate the γ and $\sqrt{\lambda}$ sets of curves. In fact, Fig. 6

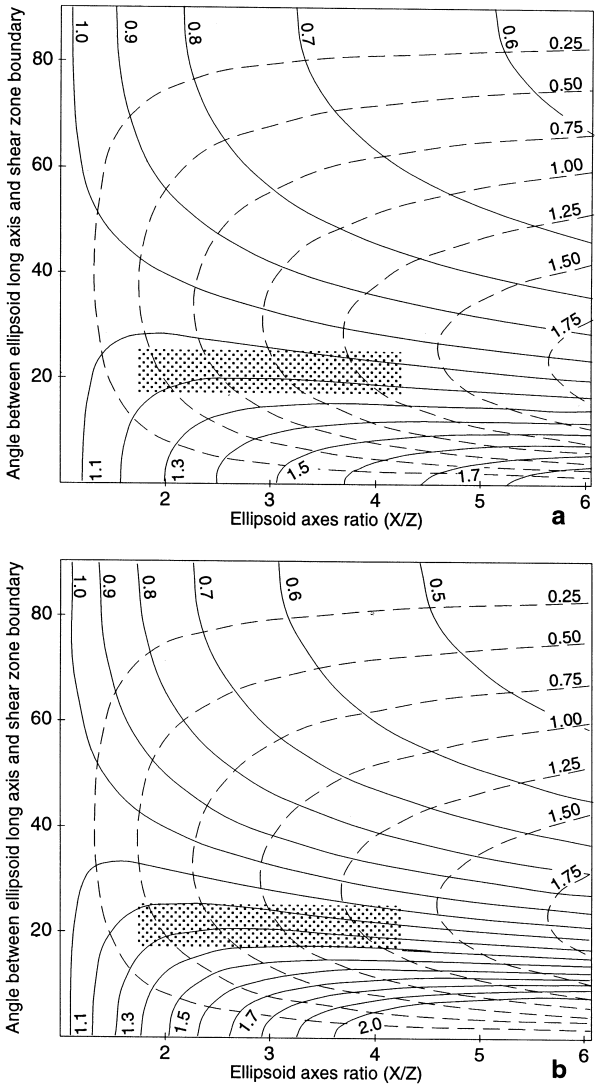

Fig. 6. Curves of equal extension $\sqrt{\lambda}$ (continuous lines) and of constant shear strain γ (dashed lines) as a function of ellipticity against inclination of the strain ellipsoid X axis to the shear zone, for the cases of triaxial strain (a) and plane ($Y = 1$) strain (b). The plots of the prolate ellipsoids from the Ma cover fall in the shaded area.

shows that in the field of $\gamma = 0$, the curve $\sqrt{\lambda} = 1$ (i.e. M_3 becomes the identity matrix) indicates an ellipticity greater than 1. Equations giving the lengths of the principal axes of the ellipsoid and the orientation of the long axis from a displacement matrix have been drawn from Jaeger (1956, p. 34).

A critical point in the application of the above method is represented by the angle between the X axis of the ellipsoid and the shear zone. On the basis of the arguments that have been presented, a range of between 18° and 25° was adopted.

Starting from a 20% mean compaction (M_1 matrix), followed by a 15% LPS (M_2 matrix), two different plots have been drawn; in the first one (Fig. 6a) the M_3 matrix represents a triaxial increment, while in the second (Fig. 6b) the incremental strain is plane ($Y = 1$). In both cases the oblate ellipsoids from the Ma cover fall in the field bounded by $0.5 \leq \gamma \leq 1.4$ and

show an extension parallel to the shear direction; the extension is higher with plane strain ($1.1 \leq \sqrt{\lambda} \leq 1.4$) than with triaxial strain ($1.1 \leq \sqrt{\lambda} \leq 1.25$).

To choose the best factorization for our bulk strain, two different paths (assuming plane and triaxial strain, respectively) have been calculated, by combining in the M_3 matrix all possible pairs of γ and $\sqrt{\lambda}$ values; each time a 0.25 and 0.1 increment for γ and $\sqrt{\lambda}$, respectively, was applied.

The results have been plotted on a Flinn diagram; comparison with data from Ma indicates that the best fit is obtained when a plane strain mechanism is adopted: simulations with low shear strain ($0.75 \leq \gamma \leq 1$) coupled with extension in the range between 1.1 and 1.4 fit 75% of the oblate strain data.

In the case of plane strain the simultaneous superposition in three dimensions of pure shear and simple shear is represented by (see the Appendix):

$$M_3 = \begin{bmatrix} \sqrt{\lambda} & 0 & \dfrac{\gamma\left(\sqrt{\lambda} - \frac{1}{\sqrt{\lambda}}\right)}{\ln\sqrt{\lambda} - \ln\frac{1}{\sqrt{\lambda}}} \\ 0 & 1 & 0 \\ 0 & 0 & \frac{1}{\sqrt{\lambda}} \end{bmatrix}. \qquad (3)$$

As previously remarked, the attitude of the crustal shear zone associated with the M_3 strain increment was not horizontal. Although the difference from a strain pattern produced by horizontal shear is negligible, we introduced an 8° clockwise rotation (θ) of the shear direction in the xz plane of the reference framework. The rotation by θ° of the coordinate system around the y axis is represented in matrix form by:

$$R = \begin{bmatrix} \cos\theta & 0 & \sin\theta \\ 0 & 1 & 0 \\ -\sin\theta & 0 & \cos\theta \end{bmatrix} \qquad (4)$$

and the total tensor Q is then given by the product $(\mathrm{R}^{-1}\cdot M_3\cdot R)\cdot M_2\cdot M_1$.

The above-discussed strain increments are shown in Fig. 7. It may be remarked that, if Δ is greater than 20%, the superposition of 15% LPS (stage ii) on compaction Δ (stage i) produces prolate ellipsoids; in this case the maximum extension is parallel to the y axis of the coordinate system, although no elongation occurs in this direction. Instead, if $\Delta \leq 20\%$, the strain remains in the apparent flattening field and z becomes the direction of maximum extension.

In the next stage (iii), the simultaneous application of pure shear and simple shear leads the strain path into the apparent flattening field in any case; the directions of the maximum and intermediate extension become parallel to the x and y axes, respectively. At the end of this stage, the field covered by: (i) 10–25% compaction; (ii) 15% initial LPS; and (iii) simultaneous shear ($0.75 \leq \gamma \leq 1$) and extension in the shear direction ($1.1 \leq \sqrt{\lambda} \leq 1.4$) overlaps the field of measured oblate ellipsoids.

Finally, as the simulation proved to be successful up to this point, we also considered the last increment, which produced the 'late D_1' thrusts and folds in the

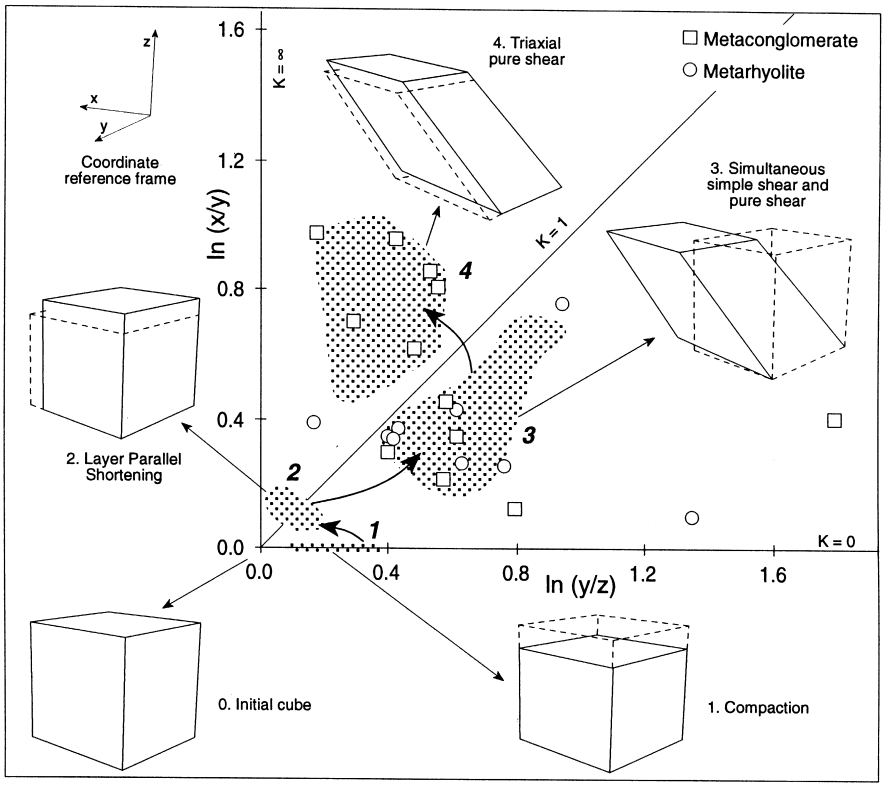

Fig. 7. Possible strain paths accompanying the pre-D_2 complex deformation history. See text for comments.

northern sector. As previously remarked, these structures were generated by shortening in the direction normal to the thrust trend (i.e. approximately parallel to the y axis of the reference framework). Indeed, the diagram shows that, to obtain ellipsoids similar to those measured in this sector, the superposition of triaxial pure shear, with 15–25% shortening parallel to y, fits all the constrictional ellipsoids that are confined to the late-D_1 deformation belt. The corresponding deformation matrix is:

$$M_4 = \begin{bmatrix} \frac{1}{\sqrt{\lambda}} & 0 & 0 \\ 0 & \lambda & 0 \\ 0 & 0 & \frac{1}{\sqrt{\lambda}} \end{bmatrix}. \quad (5)$$

During this stage (iv) the strain path moves to the apparent constriction field, triaxial prolate strains develop and the maximum extension parallel to x is maintained.

SHEATH-LIKE FOLD DEVELOPMENT SIMULATION

The strain partitioning presented in the above section is in agreement with our total strain data, but leaves open the question of whether sheath folds really do develop when using a combination of relatively low values of pure shear and simple shear.

In order to test this important point, a computer simulation model has been developed using a sinusoidal folded single layer representing the possible geometry of the basement–cover interface at the end of the early D_1 buckling. The layer deforms as a passive marker and represents the contact between two homogeneous and isotropic bodies. The mean shortening across this fold is about 15%.

The introduced perturbation consists of asymmetric folds described by a set of parametric equations giving the X, Y and Z coordinates of each point on the folded surface as a function of two parameters, m and n

$$X = A(m + \cos\ m) \quad (6a)$$

$$Y = n \quad (6b)$$

$$Z = A \cos\ m \cos\left(\frac{2\pi}{W} n\right) \quad (6c)$$

where A equals 0.6 and W is 7.9; the

$$\cos\left(\frac{2\pi}{W} n\right)$$

factor in equation (6c) has been introduced to give a smooth symmetrical curvature of the hinge line in the vertical plane. The m and n parameters have been chosen in the range from −2.2 to 4.6 and −2 to 2, respectively. (It may be of interest to remark that the A/W ratio for the symmetric curvature is about 0.076, while for the asymmetric set the maximum value reaches 0.1. These values—somewhat high, if compared with those adopted by other authors (see, e.g. Vollmer, 1988)—are constrained by the 15% *mean* shortening value that we introduced in our model. Lower A/W ratios may be obtained if less shortening is assumed; in this case, the final shape of the single fold is unmodified, but the 'perturbations' appear to be more widely scattered over the whole area.)

The above perturbation was then modified by means of an $R^{-1} \cdot M_3 \cdot R$ tensor representing the simultaneous application of the amounts of pure shear and simple shear that were calculated in the previous section:

$$\begin{bmatrix} X' \\ Y' \\ Z' \end{bmatrix} = R^{-1} \cdot M_3 \cdot R \cdot \begin{bmatrix} X \\ Y \\ Z \end{bmatrix}. \quad (7)$$

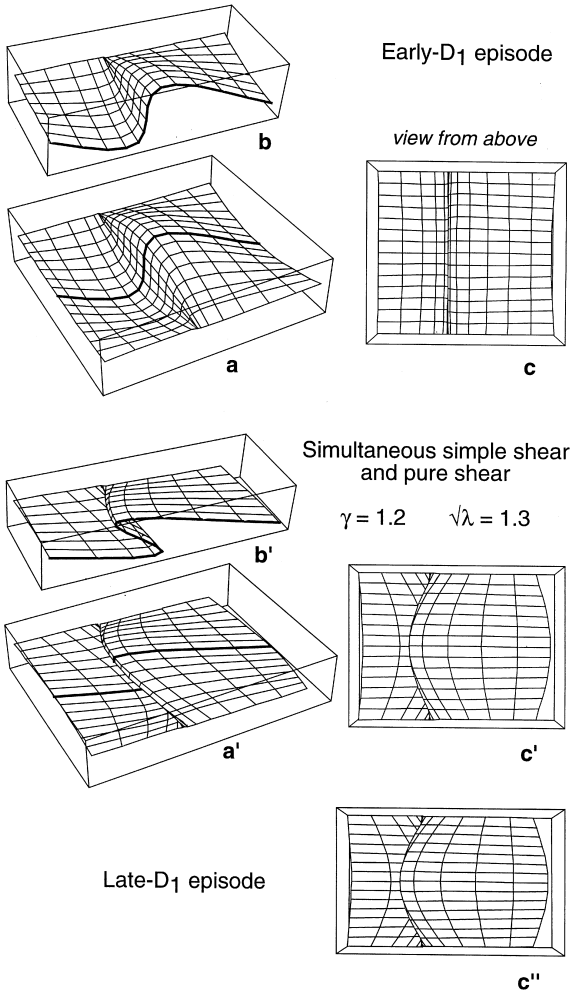

Fig. 8. Computer simulated sheath-like folds comparable to those observed in the field (see Figs 1 & 3). (a)–(c) The first episode ('early D_1') produces open, asymmetrical, non-cylindrical folds with 15% layer-parallel shortening. (a′)–(c′) The further simultaneous application of relatively low values of pure shear and simple shear generates sheath-like folds with a pronounced inverted limb. (c″) Subsequent shortening normal to the former extension direction ('late D_1' episode) slightly increases the hinge line curvature of the folds.

As shown in Fig. 8, the simulation approaches fairly well the present shape of the folds; in fact, the hinge line curvature that is obtained is greater than 90°, but this value is more closely approached when the 'late D_1' event is also taken into account (M_4 tensor). A necessary consequence of the above calculations is that, once the strain path is chosen, the geometry of the initial inhomogeneities (i.e. the 'early D_1' folds) is constrained by bulk strain data.

Our attempts to find the best fit between the folds and the final result of the simulated pattern indicate that, when relatively low values of simultaneous pure shear and simple shear are superimposed, the geometry of the initial folds should display the following characteristics:

—the shape should be asymmetrical, with a nearly vertical limb, which seems necessary to obtain a final inverted limb;

—the hinge line should be affected by undulations in the vertical plane, to obtain a final hinge line undulating in the horizontal plane.

As to the complex shape that was obtained for the 'early D_1' folds, we suggest that it might have been influenced by the irregularities of the surface between the basement and cover: in fact, both the Upper Carboniferous volcanics and the sediments were emplaced in basin-shaped depressions that were generated under a transtensional regime (Dallagiovanna *et al*., 1997a) during Late Variscan times.

POSSIBLE PRE-ALPINE ATTITUDE OF THE VARISCAN SCHISTOSITY

When comparing finite strain ellipsoids for the basement ('Esb') and cover ('Esc'), an unexpected and intriguing point is presented by their great similarity (Table 1): no great difference in total strain between cover and basement is apparent, although the basement suffered not only the Alpine, but also the Variscan orogeny, as documented by remnants of two sets of pre-Alpine foliations, accompanied by relicts of metamorphic parageneses under amphibolite-facies conditions (Cortesogno *et al*., 1995).

As previously discussed, 'Esc' units owe their present shape and attitude to Carboniferous diagenesis and the complex D_1 Alpine deformation. Hence, if we deduct from the 'Esc' the diagenetic component, we obtain the Alpine D_1 component. This component has approximately the same values in the basement; consequently, when it is subtracted from the 'Esb', the pre-Alpine components of the deformation are obtained. These consist of the diagenetic deformation of the original rhyolitic protoliths and the deformation induced by the Variscan orogeny. Assuming that the pre-Variscan and the pre-Alpine diagenetic components are about the same, it follows that when the total deformation expressed by the 'Esc' is deduced from the 'Esb', the Variscan component of the strain alone is obtained.

We should point out here that the D_2 Alpine deformation of the cover was produced on a set of planes (S_0) that were initially horizontal, and that if the above subtraction were operated on 'Esc', a sphere would obviously result. Because the 'Esb' is very similar to 'Esc', if a horizontal attitude is assumed also for the pre-Alpine schistosity, the absurd conclusion is reached that the Variscan orogeny did not produce any apparent deformation. Thus, in our opinion, the only way to explain the high degree of similarity between all the ellipsoids is to conclude that, before the Alpine episodes, the pre-Alpine foliation of the basement was inclined. No more conclusions can safely be drawn, except that the attitude of the foliation was about the same all over the investigated area; considerable differences in its dip or inclination would have led to highly differing ellipsoids.

CONCLUSIONS

The principal aim of the present work was not only to gain a better understanding of the deformation history of a sector of the Ligurian Alps, but also to verify whether and how bulk strain measurements can be more widely exploited. Along these lines, a possible model for the strain history was first deduced from geological data; subsequently, bulk strain measurements were factorized, applying strain increments consistent with the model; finally, we verified that both the sequence of deformation steps and the values calculated for each increment are suitable for producing the observed structures.

Geological data indicate that during the first, complex Alpine episode (D_1), sheath-like folds involving both the pre-Namurian basement and its Upper Carboniferous cover were generated in the lowest unit of a Penninic nappe pile. On the basis of stratigraphic, petrographic and structural analysis (kinematic indicators, geometry and attitude of the different sets of foliation, and time relations between folding and thrusting), it was deduced that the sheath-like folds were probably generated within a gently dipping shear zone. As to the strain regime, a combination of pure shear and simple shear was assumed in order to account for: (i) the many different sense of shear indicators; (ii) the depth of about 30 km at which deformation developed; and (iii) the low values of γ calculated from total strain data.

In order to obtain the initial inhomogeneity necessary for the subsequent development of sheath-like structures, a hypothetical 'early D_1' deformation producing open, asymmetric, non-cylindrical folds was introduced. The model was completed by considering the effects of both diagenetic pre-Alpine compaction, and strain connected with a 'late D_1' event which pro-

duced back-folding and thrusting. On such bases, we defined a coordinate system in the deformed state with the z axis vertical, y normal to the regional trend of the stretching lineation L_1, and x parallel to it. Strain factorization was performed by the sequential multiplication of four incremental strain matrices, representing:

(a) pre-tectonic compaction ranging from 10 to 25% in the z direction;
(b) coaxial plane strain with 15% shortening along x (layer-parallel shortening), related to the early D_1 open folding;
(c) contemporaneous superposition of layer-parallel simple shear and pure shear achieved in a crustal-scale shear zone (relevant calculations are presented in the Appendix);
(d) shortening normal to the stretching lineation direction, following the stacking of the upper nappes on to Ma.

Comparison of the above strain factorization with the geological framework has allowed us to verify their mutual compatibility.

Finally, a computer simulation was successful in showing that the proposed strain path (within the range of relatively low values of simultaneous pure shear and simple shear, consistent with bulk strain data) is actually suitable for producing sheath-like folds similar to those observed.

Acknowledgements—The authors wish to thank P. J. Hudleston, D. Schultz-Ela and F. W. Vollmer for reviewing the manuscript and for helpful criticism; in particular, the suggestion that led to the development of a computer simulation of sheath folds by simultaneous superposition of simple and pure shear strain is gratefully acknowledged. The research was supported by M.U.R.S.T. and C.N.R. grants.

REFERENCES

Cabella, R., Cortesogno, L., Dallagiovanna, G., Gaggero, L. and Vanossi, M. (1991) Nuovi dati sui terreni permo-carboniferi delle Alpi Liguri centro-occidentali. *Bollettino del Museo Regionale di Scienze Naturali, Torino* **9,** 119–139.

Cobbold, P. R. and Quinquis, H. (1980) Development of sheath folds in shear regimes. *Journal of Structural Geology* **2,** 119–126.

Cortesogno, L., Dallagiovanna, G., Gaggero, L., Seno, S. and Vanossi, M. (1995) Nuovi dati sul basamento e sul tegumento carbonifero dell'Unitá di Mallare (Brianzonese intermedio-interno, Alpi Liguri). *Atti Ticinensi di Scienze della Terra* **3,** 65–82.

Cortesogno, L., Dallagiovanna, G., Gaggero, L. and Vanossi, M. (1993) Elements of the Palaeozoic History of the Ligurian Alps. In *Pre-Mesozoic Geology in the Alps*, eds J. F. Von Raumer and F. Neubauer, pp. 257–277. Springer, Berlin.

Coward, M. P. and Kim, J. H. (1981) Strain within thrust sheets. In *Thrust and Nappe Tectonics*, eds K. R. McClay and N. J. Price, pp. 275–292. Geological Society of London Special Publication, **9**.

Dallagiovanna, G., Seno, S. and Vanossi, M. (1997b) An example of the Alpine structural evolution of the Penninic zone in the Ligurian Alps: tectonics of the Barbassiria area. *Eclogae Geologicae Helvetiae* **90,** 337–344.

Dallagiovanna, G., Seno, S. and Vanossi, M. (1997a) Strain models and palaeogeographic restorations from bulk strain data in the Pennidic domain of the Ligurian Alps. *Terra Nova (Abstract Supplement 1)* **9,** 374–375.

Dunnet, D. (1969) A technique of finite strain analysis using elliptical particles. *Tectonophysics* **7,** 117–136.

Erslev, E. A. (1988) Normalized centre-to-centre strain analysis of packed aggregate. *Journal of Structural Geology* **10,** 201–209.

Erslev, E. A. and Ge, H. (1990) Least-squares centre-to-centre and mean object ellipse fabric analysis. *Journal of Structural Geology* **12,** 1047–1059.

Fisher, R. V. and Schmincke, H.-U. (1984) *Pyroclastic Rocks*. Springer, Berlin.

Flinn, D. (1978) Construction and computation of three-dimensional progressive deformations. *Journal of the Geological Society of London* **135,** 291–305.

Fossen, H. and Tikoff, B. (1993) The deformation matrix for simultaneous simple shearing, pure shearing and volume change, and its application to transpression–transtension tectonics. *Journal of Structural Geology* **15,** 413–422.

Frei, W., Heitzmann P. and Lehner P. (1990) Swiss NFP-20 research program of the deep structure of the Alps. In *Deep Structure of the Alps*, eds F. Roure, P. Heitzmann and R. Polino, pp. 29–46. Mémoires de la Société Géologique de France, Paris **156**; Mémoires de la Société Géologique de Suisse, Zurich **1**; Società Geologica Italiana, Roma, Special Volume **1**.

Fry, N. (1979) Random point distributions and strain measurements in rocks. *Tectonophysics* **60,** 89–105.

Hanna, S. S. and Fry, N. (1979) A comparison of methods of strain determination in rocks from southwest Dyfed (Pembrokeshire) and adjacent areas. *Journal of Structural Geology* **1,** 155–162.

Jaeger, J. C. (1956) *Elasticity, Fracture and Flow*. Methuen, London.

Lisle, R. J. (1977) Estimation of the tectonic strain ratio from the mean shape of the deformed elliptical markers. *Geologie en Mijnbouw* **56,** 140–144.

Loup, B. (1992) Mesozoic subsidence and stretching models of the lithosphere in Switzerland (Jura, Swiss Plateau and Helvetic realm). *Eclogae Geologicae Helvetiae* **85,** 541–572.

Milton, N. J. (1980) Determination of the strain ellipsoid from measurements on any three sections. *Tectonophysics* **64,** 19–27.

Ramberg, H. (1975) Particle paths, displacement and progressive strain applicable to rocks. *Tectonophysics* **28,** 1–38.

Ramberg, H. (1976) Superposition of homogeneous strain and progressive deformation in rocks. *Bulletin of the Geological Institute of the University of Uppsala* **6,** 35–67.

Ramsay, J. G. (1967) *Folding and Fracturing of Rocks*. McGraw-Hill, New York.

Ramsay, J. G. and Huber, M. I. (1987) *The Techniques of Modern Structural Geology. Volume 2: Folds and Fractures*. Academic Press, London.

Rittenhouse, G. (1971) Pore-space reduction by solution and cementation. *Bulletin of the American Association of Petroleum Geologists* **55,** 80–91.

Sanderson, D. J. (1976) The superposition of compaction and plane strain. *Tectonophysics* **30,** 35–54.

Sanderson, D. J. (1982) Models of strain variation in nappes and thrust sheets: a review. *Tectonophysics* **88,** 201–233.

Skjernaa, L. (1989) Tubular folds and sheath folds: definitions and conceptual models for their development, with examples from Grapesvare area, northern Sweden. *Journal of Structural Geology* **11,** 689–703.

Tikoff, B. and Fossen, H. (1993) Simultaneous pure and simple shear: the unifying deformation matrix. *Tectonophysics* **217,** 267–283.

Vanossi, M. (1991) *Guide Geologiche Regionali: Alpi Liguri*. BE-MA, Milano.

Vanossi, M., Cortesogno, L., Galbiati, B., Messiga, B., Piccardo, G. B. and Vannucci, R. (1986) Geologia delle Alpi Liguri: dati, problemi, ipotesi. *Memorie della Società Geologica Italiana* **28,** 5–75.

Vollmer, F. W. (1988) A computer model of sheath-nappes formed during crustal shear in the Western Gneiss Region, central Norwegian Caledonides. *Journal of Structural Geology* **10,** 735–743.

Wheeler, J. (1986) Average properties of ellipsoidal fabrics: implications for two- and three-dimensional methods of strain analysis. *Tectonophysics* **126,** 259–270.

APPENDIX

Simultaneous superposition in three dimensions of pure shear and simple shear

The simultaneous superposition of pure shear and simple shear can be treated by considering the displacements in terms of rate of change in longitudinal strain

$$\left(\dot{\varepsilon} \equiv \frac{\mathrm{d}\varepsilon}{\mathrm{d}t}\right)$$

and in shear strain

$$\left(\dot{\gamma} \equiv \frac{\mathrm{d}\gamma}{\mathrm{d}t}\right).$$

In three dimensions the rates of change of the displacement components at a point in a homogeneously deforming body are related to the rate of change of strain by means of the following differential equations:

pure shear

$$\begin{bmatrix}\dot{x}\\ \dot{y}\\ \dot{z}\end{bmatrix} = \begin{bmatrix}\dot{\varepsilon}_x & 0 & 0\\ 0 & \dot{\varepsilon}_y & 0\\ 0 & 0 & \dot{\varepsilon}_z\end{bmatrix}\begin{bmatrix}x\\ y\\ z\end{bmatrix}; \tag{A1}$$

simple shear, when shear direction coincides with the x axis

$$\begin{bmatrix}\dot{x}\\ \dot{y}\\ \dot{z}\end{bmatrix} = \begin{bmatrix}0 & 0 & \dot{\gamma}\\ 0 & 0 & 0\\ 0 & 0 & 0\end{bmatrix}\begin{bmatrix}x\\ y\\ z\end{bmatrix}. \tag{A2}$$

In terms of rates of change of the displacement components, the simultaneous superposition of pure shear and simple shear in a common coordinate system is described by Ramberg (1975, 1976):

$$\begin{bmatrix}\dot{x}\\ \dot{y}\\ \dot{z}\end{bmatrix} = \begin{bmatrix}\dot{\varepsilon}_x & 0 & \dot{\gamma}\\ 0 & \dot{\varepsilon}_y & 0\\ 0 & 0 & \dot{\varepsilon}_z\end{bmatrix}\begin{bmatrix}x\\ y\\ z\end{bmatrix}. \tag{A3}$$

where $\dot{\varepsilon}_x$, $\dot{\varepsilon}_y$, $\dot{\varepsilon}_z$ and $\dot{\gamma}$ are the instantaneous strain rates. Ramberg (1976) has shown that, according to the theory of differential equations, equation (A3) has the solution:

$$\begin{bmatrix}x\\ y\\ z\end{bmatrix} = \begin{bmatrix}c_{11} & c_{12} & c_{13}\\ c_{21} & c_{22} & c_{23}\\ c_{31} & c_{32} & c_{33}\end{bmatrix}\begin{bmatrix}\exp(\dot{\varepsilon}_x t)\\ \exp(\dot{\varepsilon}_y t)\\ \exp(\dot{\varepsilon}_z t)\end{bmatrix}. \tag{A4}$$

$\dot{\varepsilon}_x$, $\dot{\varepsilon}_y$, $\dot{\varepsilon}_z$ are the three eigenvalues of the coefficient matrix (A3) and c_{ij} are constants related to the corresponding eigenvectors. Following Ramberg (1976), equation (A4) becomes

$$\begin{bmatrix}x'\\ y'\\ z'\end{bmatrix} = \begin{bmatrix}x+\dfrac{\dot{\gamma}}{\dot{\varepsilon}_x-\dot{\varepsilon}_z} & 0 & \dfrac{\dot{\gamma}}{\dot{\varepsilon}_x-\dot{\varepsilon}_z}z\\ 0 & y & 0\\ 0 & 0 & z\end{bmatrix}\begin{bmatrix}\exp(\dot{\varepsilon}_x t)\\ \exp(\dot{\varepsilon}_y t)\\ \exp(\dot{\varepsilon}_z t)\end{bmatrix} \tag{A5}$$

x', y', z' being the final coordinates of a given point initially located at x, y, z after displacement due to simultaneous superposition of pure shear and simple shear. Equation (A5) can be displayed in a more convenient form to show the finite deformation and the geometrical configuration achieved after a lapse of time t:

$$\begin{bmatrix}x'\\ y'\\ z'\end{bmatrix} = \begin{bmatrix}\exp(\dot{\varepsilon}_x t) & 0 & \dfrac{\dot{\gamma}(\exp(\dot{\varepsilon}_x t)-\exp(\dot{\varepsilon}_z t))}{\dot{\varepsilon}_x-\dot{\varepsilon}_z}\\ 0 & \exp(\dot{\varepsilon}_y t) & 0\\ 0 & 0 & \exp(\dot{\varepsilon}_z t)\end{bmatrix}\begin{bmatrix}x\\ y\\ z\end{bmatrix}. \tag{A6}$$

Equation (A6) shows the displacements as a continuous function of time.

When the rate of strain is constant in space and time, hence $\varepsilon_i = \dot{\varepsilon}_i t$ is the finite natural strain ($\varepsilon_i = \ln\sqrt{\lambda_i}$) and $\sqrt{\lambda_i} = \exp(\dot{\varepsilon}_i t)$ is the finite elongation; $\dot{\varepsilon}_i$ is the strain rate in direction i due to longitudinal strain, as $\dot{\gamma}$ is the strain rate due to simple shear $\gamma = \dot{\gamma}t$ is the finite shear strain (Jaeger, 1956; Coward and Kim, 1981).

As

$$\dot{\gamma} = \frac{\gamma}{t} \text{ and } \dot{\varepsilon}_i t = \ln\sqrt{\lambda_i}$$

$$\frac{\dot{\gamma}}{\dot{\varepsilon}_x - \dot{\varepsilon}_z}$$

becomes

$$\frac{\gamma}{\dot{\varepsilon}_x t - \dot{\varepsilon}_z t} = \frac{\gamma}{\ln\sqrt{\lambda_x} - \ln\sqrt{\lambda_z}}. \tag{A7}$$

Introducing these finite strains into equation (A6) yields:

$$\begin{bmatrix}x'\\ y'\\ z'\end{bmatrix} = \begin{bmatrix}\sqrt{\lambda_x} & 0 & \dfrac{\gamma(\sqrt{\lambda_x}-\sqrt{\lambda_z})}{\ln\sqrt{\lambda_x}-\ln\sqrt{\lambda_z}}\\ 0 & \sqrt{\lambda_y} & 0\\ 0 & 0 & \sqrt{\lambda_z}\end{bmatrix}\begin{bmatrix}x\\ y\\ z\end{bmatrix} \tag{A8}$$

If we account for incompressibility and for axial symmetric longitudinal strain, that is

$$\sqrt{\lambda_x} = \sqrt{\lambda_y} = \sqrt{\lambda}$$

and

$$\sqrt{\lambda_z} = \frac{1}{\lambda},$$

at the moment of contemporaneous superposition of pure shear and simple shear the deformation matrix (A8) can be expressed in terms of λ and γ:

$$\begin{bmatrix}x'\\ y'\\ z'\end{bmatrix} = \begin{bmatrix}\sqrt{\lambda} & 0 & \dfrac{\gamma\left(\sqrt{\lambda}-\dfrac{1}{\lambda}\right)}{\ln\sqrt{\lambda}-\ln\dfrac{1}{\lambda}}\\ 0 & \sqrt{\lambda} & 0\\ 0 & 0 & \dfrac{1}{\lambda}\end{bmatrix}\begin{bmatrix}x\\ y\\ z\end{bmatrix}. \tag{A9}$$

The above 3×3 deformation matrix is able to describe the displacement in three dimensions of any point in a rock deforming by homogeneous strain at a constant strain rate, and can be used to deform a sphere to produce the strain ellipsoid; the corresponding equation has been solved for various values of λ and γ and the resulting curves have been plotted in Fig. 6(a). In the case of plane strain (λ and γ curves plotted in Fig. 6b), longitudinal strains are

$$\sqrt{\lambda_x} = \sqrt{\lambda},\ \sqrt{\lambda_y} = 1,\ \sqrt{\lambda_z} = \frac{1}{\sqrt{\lambda}},$$

and the displacement is described by equation

$$\begin{bmatrix}x'\\ y'\\ z'\end{bmatrix} = \begin{bmatrix}\sqrt{\lambda} & 0 & \dfrac{\gamma\left(\sqrt{\lambda}-\dfrac{1}{\lambda}\right)}{\ln\sqrt{\lambda}-\ln\dfrac{1}{\lambda}}\\ 0 & 1 & 0\\ 0 & 0 & \dfrac{1}{\sqrt{\lambda}}\end{bmatrix}\begin{bmatrix}x\\ y\\ z\end{bmatrix}. \tag{A10}$$

These matrices give finite deformation identical to those obtained in a slightly different form by Fossen and Tikoff (1993) and Tikoff and Fossen (1993).